MATERIALS SCIENCE

Defect-engineered epitaxial $VO_{2\pm\delta}$ in strain engineering of heterogeneous soft crystals

Yiping Wang,[1] Xin Sun,[2] Zhizhong Chen,[1] Zhonghou Cai,[3] Hua Zhou,[3] Toh-Ming Lu,[2] Jian Shi[1]*

The success of strain engineering has made a step further for the enhancement of material properties and the introduction of new physics, especially with the discovery of the critical roles of strain in the heterogeneous interface between two dissimilar materials (for example, FeSe/$SrTiO_3$). On the other hand, the strain manipulation has been limited to chemical epitaxy and nanocomposites that, to a large extent, limit the possible material systems that can be explored. By defect engineering, we obtained, for the first time, dense three-dimensional strongly correlated $VO_{2\pm\delta}$ epitaxial nanoforest arrays that can be used as a novel "substrate" for dynamic strain engineering, due to its metal-insulator transition. The highly dense nanoforest is promising for the possible realization of bulk strain similar to the effect of nanocomposites. By growing single-crystalline halide perovskite $CsPbBr_3$, a mechanically soft and emerging semiconducting material, onto the $VO_{2\pm\delta}$, a heterogeneous interface is created that can entail a ~1% strain transfer upon the metal-insulator transition of $VO_{2\pm\delta}$. This strain is large enough to trigger a structural phase transition featured by PbX_6 octahedral tilting along with a modification of the photoluminescence energy landscape in halide perovskite. Our findings suggest a promising strategy of dynamic strain engineering in a heterogeneous interface carrying soft and strain-sensitive semiconductors that can happen at a larger volumetric value surpassing the conventional critical thickness limit.

INTRODUCTION

With the presence of strain, a lattice perturbation away from the ground state, it is widely accepted that novel material phases with strain-induced new properties (*1*–*6*) and improvement of its intrinsic capabilities (*7*–*11*) can be obtained. Together with temperature and composition, the third component in a material phase diagram, strain (positive and negative pressure) has become an equally indispensable aspect for the engineering of material and thus ushering in the field of strain engineering. More fortunately, materials on smaller scales preserve a drastically increased elastic strain limit (*12*) that ensures a promising and applicable prospective of the field. Among various techniques of strain manipulation, chemical epitaxial strain has been most matured over the past years where it is possible to control the strain by carefully choosing the substrate and film combination (*13*, *14*). However, the maximum thickness of the strained overlayer is severely limited by interface thermodynamics to several nanometers with ~1% strain (*15*), a value necessary for achieving real desirable property modification. A smart solution to this dilemma has been the creation of nanocomposite materials (*16*–*18*) where two similar but insoluble phases are grown on a third chemically similar substrate. The spinodal decomposition of the film during growth results in nanopillars with decreased scale and increased elastic limit, thus greatly augmenting the strained layer thickness to micrometer scale. However, in another perspective, the addition of a third component in nanocomposites further tightens the pairing requirement, and consequently, most nanocomposite materials consist only of oxides.

The effectiveness of strain engineering in either epitaxial films or nanocomposites via misfit strain largely relies on the structural and chemical similarity of the film and substrate (or matrix and pillar). An isostructural interface between film and substrate (or between matrix and pillar) is often needed to deliver more than ~1% elastic strain. However, recent advancements in several emerging heterogeneous materials system [for example, FeSe/$SrTiO_3$ (*19*)] show that strain engineering may be very demanded in the material (*20*, *21*) that has a completely different chemistry and crystal symmetry/structure than the host material. In this scenario, how strain engineering should be implemented and how the target crystal responds to strain perturbations remain poorly understood.

Here, we propose a novel substrate composing of defect-engineered vertically aligned VO_2 nanowire forest and a new heterogeneous interface VO_2/soft crystals for the purpose of elastic strain engineering. On the one hand, the metal-insulator transition (MIT) of VO_2 ensures an abrupt dynamical structural change (*22*, *23*) that is expected to be translated to the strain-sensitive material on top. A heterogeneous interface between VO_2 and soft crystal (*24*) halide perovskite [an emerging optoelectronic material that may lead to versatile properties via strain engineering (*2*, *25*, *26*)] is developed to test the strain engineering concept in halide perovskite. On the other hand, the dense array of nanowires could produce a similar effect as the nanopillars in nanocomposites, which is possible for the realization of strain at bulk with more flexibility on material choice.

The realization of this substrate would prove challenging enough due to the complicated thermodynamics of vanadium-oxygen compounds. First, the low vapor pressure of transition metal vanadium almost rules out one of the most common growth strategies for aligned nanowires—the foreign metal-catalyzed vapor-liquid-solid (VLS) approach (*27*, *28*)—because it is fairly difficult to form an oversaturated eutectic liquid with the other metal catalyst of low vapor pressure (for the purpose of minimizing catalyst's unintentional doping effect on VO_2) at moderate temperature. Second, a VO_2 nanowire/micron beam itself poses much complexity because tiny environmental changes, that is, strain, temperature, and composition, will end up with a different phase transformation and therefore different structural change (*29*–*31*). Therefore, to fully realize the VO_2 nanoforest substrate, a unique design and thorough understanding of the controllable growth process are urgently needed. To tackle this problem, in this work, by taking advantage of a stoichiometric defect, we report the growth of a

[1]Department of Materials Science and Engineering, Rensselaer Polytechnic Institute, Troy, NY 12180, USA. [2]Department of Physics, Applied Physics, and Astronomy Rensselaer Polytechnic Institute, Troy, NY 12180, USA. [3]X-ray Science Division, Argonne National Laboratory, Lemont, IL 60439, USA.
*Corresponding author. Email: shij4@rpi.edu

vertically aligned M2-phase VO_2 hybrid nanowire array that could potentially circumvent the pairing requirements for common nanocomposites and, at the same time, introduces the dynamic bulk strain by triggering the VO_2 phase transformation. By controlling the growth temperature and oxygen vapor pressure, a dense array of VO_2 nanowire arrays can be obtained by a template growth from V_2O_5 droplets. Revealed by Raman spectroscopy, the as-grown freestanding VO_2 nanoforest stabilizes itself in the M2 phase as a result of the oxygen-rich template of V_2O_5, different from the commonly observed M1 phase. The M2-R phase transition renders a larger lattice contraction compared to the conventional M1-R trend and thus is more promising for effective strain engineering. Our findings also shed light on the third component besides temperature and strain that can modulate the phase of VO_2 in a more facile manner.

As a second step for the demonstration of the effectiveness of strain engineering in a chemically and structurally dissimilar material from VO_2, single-crystalline halide perovskite $CsPbBr_3$ crystallite is deposited onto the VO_2. As an emerging semiconductor material initially in photovoltaics (*32*, *33*), halide perovskite has now attracted much attention in various other fields (*34*–*38*). New properties including ferroelectricity and topological insulators have been suggested under adequate strain (*2*). Here, we show that by using the VO_2 substrate, it is possible to strain halide perovskite for as large as 1% dynamically to trigger a PbX_6 octahedral tilting–associated phase transition of the perovskite itself with a modified electronic band structure, despite the existence of an incoherent heterogeneous interface. Our findings serve both as an experimental investigation of the strain engineering by VO_2 and also, at the same time, as an illustration on the behavior of inorganic halide perovskite under significant nonhydrostatic pressure. It is believed that the successful strain engineering from this heterogeneous interface may significantly rely on the mechanical softness of halide perovskite crystals.

The design schematics of the VO_2 nanowire hybrid material system are depicted explicitly in Fig. 1. Among most available substrates, sapphire (Al_2O_3) has been chosen as the appropriate candidate for the growth of aligned VO_2 arrays due to the good chemical wetting and the flexible choice of the various miscut facets and crystallographic directions. The epitaxial growth of nanostructured multivalent vanadium oxide has been shown successful on the c-plane (0001) sapphire substrate (*39*), and it is generally accepted that similar growth on other miscut facets [that is, a-plane ($11\bar{2}0$), m-plane ($10\bar{1}0$), and r-plane ($1\bar{1}02$)] results in a freestanding strain-free VO_X compound. Figure 1A shows the tilted view of a hexagonal prism of a sapphire crystal where the r-plane is intentionally placed horizontally. Other conventional facets (for example, the basal c-plane) can also be visualized easily on the prism. The idea of growing three-dimensional (3D) VO_2 nanowire arrays stems from the already-established fact that in-plane VO_2 nanowire with sixfold symmetry (*39*) can be easily obtained on the c-plane, as shown by the VO_2 nanowire alignment indicated on the basal c-plane. Early research has also shown that the as-grown VO_2 on the c-plane follows the $<11\bar{2}0>$ directions (*39*). As per the information above, we can reasonably deduce that if one of the three VO_2 alignments on c-plane is translated onto the corresponding r-plane of sapphire, then it would then be possible to organize the VO_2 arrays along a uniform direction in a 3D manner, which is not obtainable for the 2D growth condition on the basal c-plane. The choice of r-plane sapphire can also ensure that at high nucleation rate, a denser array would be formed, whereas the better chemical wetting on the c-plane could entail a uniform film that prohibits the formation of a hybrid material.

Figure 1B further shows the idea of the VO_2 hybrid material by a combination of the strongly correlated phase change material and the strain-sensitive optically active semiconductors and, in this case, the inorganic halide perovskite $CsPbBr_3$. The dual-step formation of the VO_2 hybrid could circumvent the rigid pairing requirement for most nanocomposite materials, and the enhanced elasticity of nanowires can facilitate the formation of epitaxy even with a larger lattice mismatch. Upon the phase transition of VO_2, the coated semiconducting material will experience an abrupt compressive strain after the contraction of VO_2 nanowire along the *c* axis, as shown by exaggeration in Fig. 1B. The high density of 3D VO_2 arrays would then give rise to a significant strain value over a large volumetric area, far exceeding the conventional limit on the critical thickness of the strained layer. The crystallographic orientation and surface facets of the VO_2 nanowires are also depicted exclusively in Fig. 1B, according to the previous study on the nanowire morphology (*40*).

After the reasoning above, the exact phase transition of VO_2 would directly affect the strain exerted onto the coating layer, which is further discussed in the phase diagram of VO_2 in Fig. 1C, adapted from previous reports investigating the possible ways to affect MIT

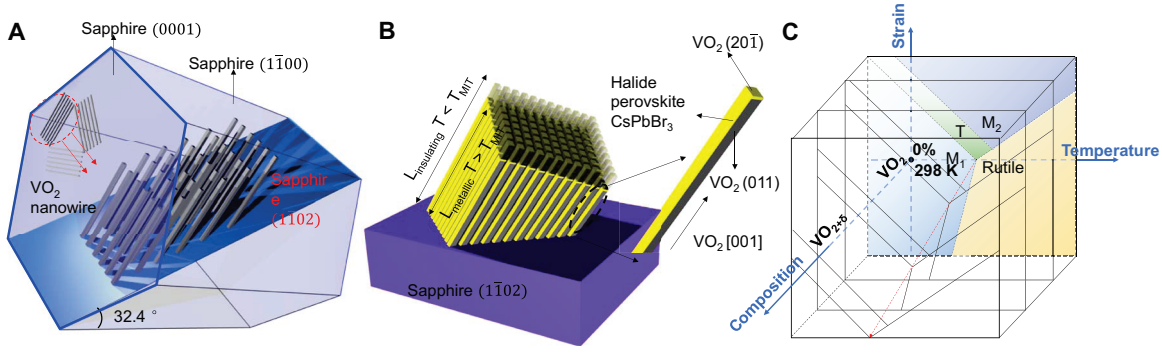

Fig. 1. Design schematics of strain engineering at heterogeneous interface via defect-engineered epitaxial strongly correlated oxide crystals. (**A**) Schematics showing the relative crystallographic orientation of the VO_2 nanowire and the hexagonal prism of the sapphire crystal. The in-plane growth of the VO_2 nanowires on the basal c-plane can be translated to the r-plane, which results in a uniform array of vertically aligned nanowires. (**B**) Schematics showing the VO_2 hybrid material upon the MIT. The nanoforest would experience an abrupt contraction along the *c* axis at MIT, which can effectively strain the crystal on top ($CsPbBr_3$ in this case). The crystallographic orientation and surface facets of the individual VO_2 nanowire are also labeled. (**C**) A 3D phase diagram of VO_2 including the change in temperature, strain, and composition. New phases, such as M2 and T, can be introduced by applying strain or slightly changing the stoichiometric ratio.

(*31*, *41*, *42*). For VO_2, temperature variation would trigger the MIT of VO_2 from its pristine M1 phase in room temperature to a metallic rutile phase at elevated temperature. It is also well accepted that slight environmental perturbations, such as pressure and change in component, would result in a completely different phase transition pathway by introducing the new monoclinic M2 and triclinic T phases. MIT happening at different phase pathways would entail a different lattice constant change, although the change in terms of the electric conductivity is similar. To the best of our knowledge, a 3D phase diagram that takes into account the temperature, pressure, and component has yet to be constructed despite the recent successful attempts on the 2D phase diagrams including temperature and strain/component. Shown in Fig. 1C is the 3D phase diagram discussed above for VO_2 with the intersection of the three axes being the pristine VO_2 (without strain and perfect 1:2 ratio) at room temperature. For the strain part, the introduction of slight tensile strain would shift the VO_2 into the M2 phase at room temperature and push the MIT temperature higher. A similar effect can also be achieved by introducing an excessive oxygen ratio that ends up with a M1-T-M2-R phase change pathway. The resultant change can also be visualized by the shift of the triple-phase junction point by a change in oxygen ratio while keeping VO_2 unstrained (red dashed line). For the case of the freestanding strain-free VO_2 arrays grown on the r-plane sapphire, the modulation on the phase transition by component would then be the question of interest and would be investigated further in the following section.

RESULTS

Growth of epitaxial $VO_{2\pm\delta}$ nanoforest

The specific growth of 3D VO_2 nanowire arrays is described in Fig. 2. The multivalent nature of vanadium gives rise to additional challenges for the growth of intermediate state of VO_2 between the lower-temperature, oxygen-sufficient phase of V_2O_5 and higher-temperature, oxygen-deficient phase of V_2O_3. Meanwhile, the different crystal structure and lattice mismatch of different valent VO_X components on r-plane sapphire could complicate the growth further. To tackle the challenges mentioned above, we designed a two-step, self-templated growth of VO_2 using V_2O_5 as precursor, as shown in Fig. 2A, with the rest of growth details with regard to the exact setup included in the Supplementary Materials. In general, the growth includes the (i) growth of V_2O_5 droplets as templates on the surface of r-plane sapphire and (ii) the growth of VO_2 nanowire from the droplet into aligned nanowire arrays. For the first stage, a 20:80% oxygen/argon (volumetric ratio) carrier gas is maintained to create an oxygen-rich environment that prevents the formation of vanadium with reducing (+3 and +4) valence states. The much higher temperature (1163 K) than the melting point of V_2O_5 would, on the other hand, prohibit the large-scale growth of V_2O_5 but rather leaves the substrate with melted V_2O_5 droplets. At the second stage of the growth, the oxygen supply is abruptly cut off, and the growth temperature also slightly lowered to provide a larger supersaturation for the growth of VO_2. During this stage, the presence of the V_2O_5 droplets would serve as a natural

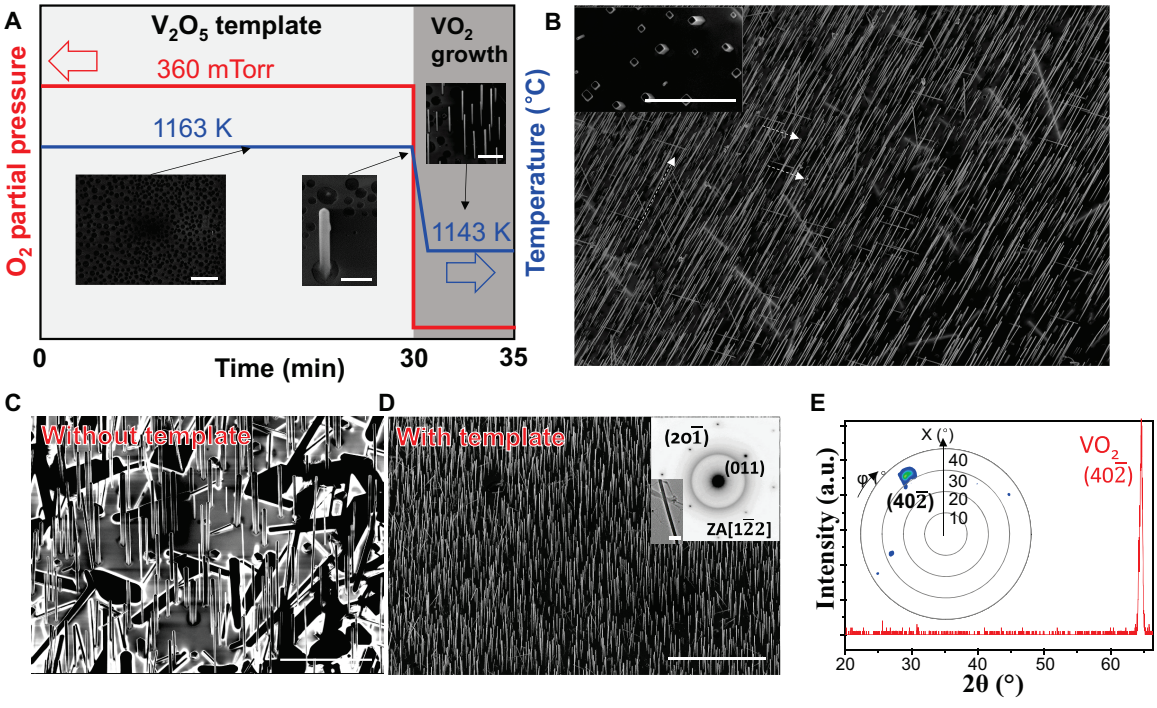

Fig. 2. Growth and structural analysis of epitaxial $VO_{2\pm\delta}$ array on r-plane sapphire. (**A**) Design schematics of the two-stage growth of the VO_2 nanoforest using V_2O_5 droplets as template by varying the oxygen partial pressure and substrate temperature during the different stages. Insets show SEM images of the V_2O_5 droplets after the first stage (left), the newly nucleated VO_2 nanowire (middle), and the nucleated VO_2 nanowires with higher density (right). (**B**) Side view of the as-grown VO_2 nanoforest with the inset being the top view. The top view reveals a rectangular cross section typical for VO_2 nanowires. (**C** and **D**) Comparison of the VO_2 growth without (C) and with (D) V_2O_5 template and two-stage process. The large difference in the density of nanowires and the decrease in the unwanted in-plane growth can be easily identified. Inset of (D), TEM image and diffraction pattern of a single VO_2 nanowire. (**E**) Pole figure of the as-grown nanoforest. Only one asymmetric pole of (40$\bar{2}$) of VO_2 at χ = 33° can be collected. The asymmetric pole is consistent with the oblique angle of the VO_2 nanoforest and the angle between the c-plane and r-plane sapphire. The combining θ-2θ scan at the pole figure geometry shows that only one peak from VO_2 exists. a.u., arbitrary units. Scale bars, 10 μm (A, left), 2 μm (A, middle), 5 μm (A, right), 40 μm (B), 10 μm (B, inset), 30 μm (C), 50 μm (D), and 1 μm (D, inset).

template for the VO_2 growth as a result of more adatoms adsorbed and the continuing process of oxygen loss at high temperature because pure argon is now used as carrier gas. Furthermore, because of the very short growth time (~5 min) for the second stage and the relatively low growth temperature compared to the melting temperature of V_2O_3, VO_X with a ratio very close to 1:2 can be maintained during the growth process. The scanning electron microscope (SEM) images as insets of Fig. 2A provide sound evidence for the proposed growth mechanism, where the images are taken with only the first stage of growth followed by a cut of oxygen supply and a quench of furnace temperature. The left inset of Fig. 2A shows a large-scale presence of black dots on the substrate surface that belongs to the remains of V_2O_5 droplets. At some locations of the substrate (middle and right inset), limited number of VO_2 nanowires can be seen grown from the droplet, showing the evidence of the template growth. The clean surface of the substrate other than the circular black dots also supports the proposed idea that an oxygen-rich atmosphere can effectively suppress the formation of VO_2 and V_2O_3. As the second stage of the designated process steps in, a marked change of growth result can be achieved, as shown in Fig. 2B. After ~5 min of VO_2 growth, uniform arrays of VO_2 with large coverage can be observed. The nanowires are tilted about 33° away from the normal of the substrate through measurement during the SEM characterization. The tilting angle coincides with the angle difference of the c- and r-plane, which supports the design in Fig. 1A. The inset of Fig. 2B shows the SEM image of the VO_2 array after tilting to the surface normal. The individual nanowire shows a rectangular cross section, which is typical for VO_2 nanowires grown on both silicon and c-plane sapphire substrates. Apart from the vertical growth of VO_2 from the droplet templates, very few numbers of in-plane horizontally aligned nanowires can also be seen (marked by the dashed white arrows). Their presence could be a result of the unintentional growth at the second stage of the growth and would be investigated in detail during the following Raman spectroscopy analysis.

With the two-step method mentioned above, it is also possible to control the nanowire size and density by adjusting the temperature in step 2. In general, as the substrate is moved closer to (or away from) the furnace center, the higher (lower) substrate temperature causes a smaller (larger) supersaturation that ends up with a less (more) dense nanoforest. The corresponding result is further shown in figs. S1 and S2. We can see that as the substrate temperature lowers, more in-plane growth other than the ones from template also appears, which is consistent with our nucleation hypothesis. Figure 2 (C and D) illustrates the difference between the growth under conventional one-step pure argon (Fig. 2C) and that with the designed growth process (Fig. 2D). The growth result in Fig. 2C has been the best we are able to obtain with one-step growth. It can be observed that apart from the huge density decrease of VO_2 nanowires, a significant in-plane growth appears as well. The in-plane micron beams show generally a much darker contrast compared with that of the VO_2, implying a much larger electrical conductivity, thus pointing to the possible formation of VO_2 with a high concentration of oxygen vacancy. $VO_{2-\delta}$ can still be formed despite the use of V_2O_5 as a precursor due to the high oxygen loss at elevated temperature without extra oxygen supply. The previous research (*43*) involving the VO_X growth on r-plane sapphire at much lower temperature (~900 K), also to some extent, avoids the formation of V^{3+}, however, at a cost of very limited number of nanowires obtained and the large-scale forest morphology missing. In addition, the corresponding Raman study of the as-grown nanowire in this research showed a more predominant composition of V_2O_5 due to the lower growth temperature based on an early study differentiating VO_2 and V_2O_5 nanowires (*44*). As a further confirmation of the crystal structure of the as-grown nanowire, electron diffraction (inset of Fig. 2D) in a transmission electron microscope (TEM) was performed on a single nanowire that reveals a rectangular pattern typical to the VO_2 nanowire with [001] as the growth direction, (011) as the side facets, and $(20\bar{1})$ as the top facet. With this known, pole figure characterization with the θ-2θ configuration set to the $(40\bar{2})$ pole of VO_2 was performed in Fig. 2E because $(20\bar{1})$ is a forbidden diffraction. The resultant pole figure reveals a single, asymmetric pole at $\chi = 33°$, identical to the SEM measurement. Figure 2E also shows the θ-2θ symmetric scan at the sample geometry where the pole is collected. The scan presents a single $(40\bar{2})$ peak after the single-crystalline nature of the nanoforest array. The two other poles in Fig. 2E with much reduced intensity each 90° in ϕ in relation with the primary pole can be assigned to the (320) poles of the same group of nanowires, and therefore, it is consistent with the single orientation of the nanowire forest. The x-ray pole figure analysis, which delivers more global information on the growth, also indicated a large-scale uniform growth of VO_2 nanowire arrays exactly as anticipated in Fig. 1A.

Characterization of the phase evolution of epitaxial $VO_{2\pm\delta}$ nanoforest

Despite the diffraction study, the exact phase of the as-grown VO_2 nanoforest is still undetermined because of the close lattice spacing among various possible phases. Thanks to the freestanding nature of the as-grown VO_2 nanoforest, the compositional change (*42*, *45*) becomes the only factor that is able to affect the phase change pathway. As per this consideration, Fig. 3A shows a schematic phase diagram of VO_2 with temperature and electron/hole doping as variables. With V_2O_3 (metallic at room temperature) and V_2O_5 (no MIT) as extreme cases, we can see that oxygen vacancies (electron doping) would decrease the MIT temperature and suppress the formation of other insulating phases such as M1 and T. Oxygen sufficiency (hole doping), on the other hand, would increase MIT temperature slightly and introduce the complicated M1-T-M2 insulating phase changes. The schematic lattice in each phase is also shown accompanied with the numeric values. It can be seen that the M2-R phase change produces the largest contraction along the *c* axis, thus being the most favorable candidate in our hybrid material design. Thanks to the previous systematic researches (*41*, *44*, *46*, *47*) on the phase identification of various VO_2 samples, it is found that Raman spectroscopy gives very distinctive responses to each of the VO_2 phases mentioned above. In general, the transition from M1-T-M2 would entail a gradual right shift of Raman peak of the V-O A_{1g} mode from around 610 to 630 cm^{-1} and finally 650 cm^{-1} until the metallic rutile phase completely screens out the Raman signal. Figure 3B shows the SEM image of the typical morphologies investigated in our study including the horizontally (A type) and vertically (B type) aligned VO_2 nanowires. The nanowire obtained using the conventional method on SiO_2/Si substrate was also used as a reference (not shown in the image). The resultant Raman spectra for all three cases are shown in Fig. 3C. It can be observed that compared with the M1 phase of nanowire grown on SiO_2/Si substrate with the A_g vibrational peak (*48*) at 611 cm^{-1}, the cases for A and B showed significant Raman shifts to higher frequencies (A, 630 cm^{-1}; B, 650 cm^{-1}). Consequently, an interesting conclusion is drawn for the two-step growth method that the as-grown horizontal nanowires are in the T phase, whereas the template-guided vertical nanowires are in

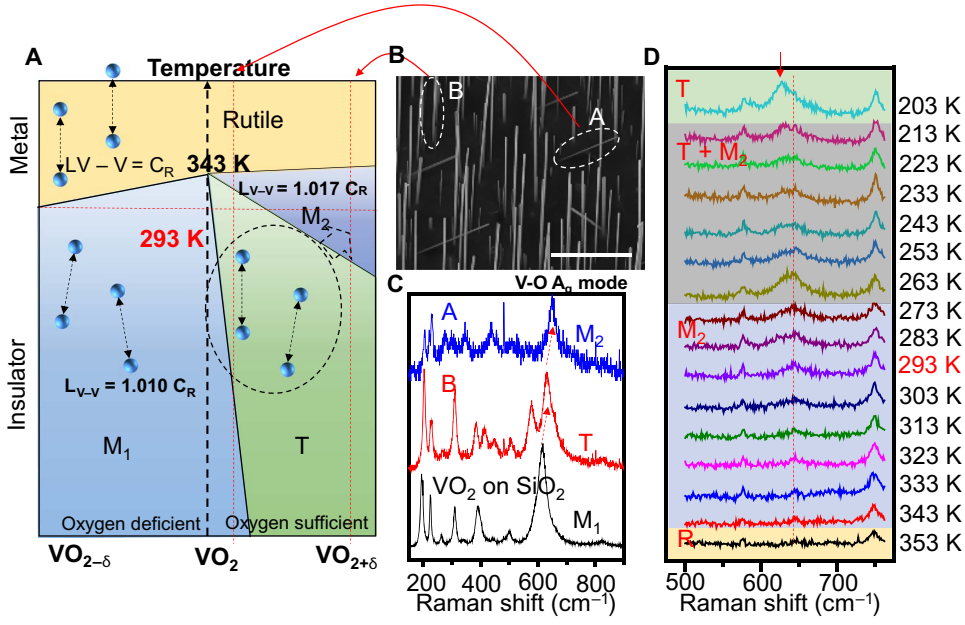

Fig. 3. Phase transition of defect-engineered epitaxial $VO_{2\pm\delta}$ forest by in situ Raman spectroscopy. (**A**) Binary phase diagram of VO_2 with changing stoichiometry and temperature. Oxygen sufficiency and deficiency modulate the phase of VO_2 and introduce new phases such as M2 and T. The schematics of the VO_2 lattice for each phase and the change of V–V bond are depicted. (**B**) Magnified SEM image of the VO_2 nanoforest showing two kinds of nanowire: horizontally aligned (type A) and vertically aligned (type B). Scale bar, 10 μm. (**C**) Raman spectra of the two types of nanowires previously described (blue and red) and also the ones grown on SiO_2/Si (black) as a reference. The three types of nanowire are in three different phases that can be identified by the V-O A_g vibrational mode. (**D**) Temperature-dependent Raman spectra of the type B VO_2 nanoforest. The as-grown nanowire undergoes a T-M2-R phase transition in the temperature window investigated.

the M2 phase. Considering the growth conditions, it is reasonable to deduce that because of the initial oxygen-rich V_2O_5 droplet, the VO_2 nanowire grown from it always remains slightly oxygen sufficient (in other words, with vanadium vacancies), therefore rendering it M2 phase. On the other hand, the unintentional growth of horizontal nanowires remains in an intermediate T phase between M1 and M2 due to the lack of an oxygen-rich template at the first place. Nonetheless, the overall growth process (more oxygen in the first stage) still makes the type A nanowire slightly sufficient in oxygen compared with the one grown on SiO_2/Si with pure argon and therefore produces the T phase for the A-type nanowire. The analysis above also rules out the possibility of Al-doping from substrate (otherwise, the horizontally aligned ones would have a more significant hole doping) into the VO_2 nanowire, which could also result in a similar hole-doping phenomenon.

To further validate our phase change hypothesis of the nanowire, we carried out a temperature-dependent Raman characterization of the vertically aligned (type B) nanowire, and the results are shown in Fig. 3D. At higher temperature (~353 K), the nanowire lost most of the Raman signal and was converted into the metallic rutile phase. Although at lower temperature, a gradual blue shift of the peak to the T phase can be observed. For a relatively large temperature window, the coexistence of two phases can be seen, which is typical for phase change materials. Both the slight increase of MIT temperature and the M2-T transition at lower temperature fit very well with the hole-doped VO_2 phase diagram drawn in Fig. 3A. Therefore, from the Raman characterization, we show that the designed growth not only results in a highly dense VO_2 nanowire array but also ends up with VO_2 of a different phase compared to conventional methods. The M2-phase VO_2 nanowire array is better suited for a strain engineering purpose for a larger lattice constant variation at MIT. To further validate our hypothesis, we deposited a 50-nm-thick amorphous $BaTiO_3$ layer by room temperature radio frequency (RF) sputtering onto the as-grown M2-phase VO_2 nanoforest, as shown in fig. S3, where the core-shell structure can be easily seen. Whereas the TEM characterization still reveals the VO_2 shell to be single crystalline (fig. S4); the corresponding Raman spectroscopy at room temperature in fig. S5 shows a significant red shift to the T phase VO_2. Considering the freestanding nature of VO_2 nanowire and the geometry of RF sputtering, as $BaTiO_3$ is deposited only on one side of the nanowire, a cantilever-like setup is formed. The nanowire would become bent if a significant strain exists in VO_2. If significant strain exists because $BaTiO_3$ is thin compared to VO_2, then the strain states would include both compressive and tensile depending on the side of the nanowire, and the Raman spectrum (the laser spot in Raman spectroscopy characterization is larger than the diameter of the nanowire) would show both blue and red shifts. Because only a red shift of the Raman spectrum is observed, the Raman peak shift is thus unlikely due to strain imposed with the deposition of $BaTiO_3$, which is likely negligible considering its relative thickness to VO_2's diameter. Furthermore, from both SEM and TEM images shown in fig. S3 (B and C), the demanded bending reflecting significant strain states was not observed. The evidence above suggest that the shift in the Raman spectrum does not come from the depositional strain of VO_2. Rather, we suggest that this can be understood by the stronger oxygen capturing capability of Ti^{4+} to balance the stoichiometric ratio of VO_2 to be less oxygen sufficient (*49*). That is to say, compared with V–O bond in VO_2, the Ti–O bond in $BaTiO_3$ is stronger, so that when $BaTiO_3$ is deposited on VO_2, the oxygen-deficient nature of $BaTiO_3$ and the already existing $VO_{2+\delta}$ will balance their oxygen stoichiometry so that oxygen diffuses from $VO_{2+\delta}$ to $BaTiO_3$. We attribute the broadening to the possible existence of two phases because the oxygen transfer may be incomplete.

Strain engineering using $VO_{2\pm\delta}$ at a heterogeneous interface with halide perovskite

With the acquisition of the defect-engineered epitaxial VO_2 nanoforest, we move a step forward to demonstrate the concept of strain engineering in a model heterogeneous crystal—halide perovskite. In addition to its completely different chemistry and structure from VO_2 and promising optoelectronic/emerging physical properties, halide perovskite's strain-modified phase diagram has been recently revealed experimentally by a high-pressure study (*50*). Finally, halide perovskite has been shown carrying very low shear moduli (*24*) (for example, 5.9 GPa for $CsPbBr_3$), suggesting that a relatively low elastic stress could induce significant strain. All these make this type of crystal a great model material to study in strain engineering. To fully reveal the fundamental physics behind the halide perovskite/VO_2 hybrid material carrying heterogeneous interfaces, we transfer the VO_2 nanowires onto the mica/NaCl substrate and grow single-crystalline $CsPbBr_3$ flakes on the nanowires under a relatively low nucleation rate.

The nanowires have been transferred onto mica/NaCl the same way as the transfer of them onto the TEM grid. By gently pressing the VO_2/sapphire on another substrate, a large number of nanowires can be transferred. Although the nanowire has been epitaxially grown on the r-plane sapphire substrate, the unique tilted growth geometry determines that the nanowire is more freestanding-like than tightly bonded to the substrate. Therefore, the transfer process will not affect the crystallinity or the phase of nanowire. The TEM image and diffraction pattern in Fig. 2 show that the transferred nanowire does not have any damage or change to the crystallinity. Moreover, the phase modulation of VO_2 in our case is realized by the oxygen stoichiometry instead of external strain; therefore, the phase of VO_2 is not supposed to be changed by transfer either. The transfer of the nanowires away from the sapphire substrate is intended to create an atmosphere that is friendly for the growth of halide perovskite on both mica and NaCl, depending on our previous understanding on the perovskite growth (*51*, *52*). To be more precise, we found that the nucleation and wetting of halide perovskite are favorable only on certain substrates [mica (*52*), NaCl (*53*), and $SrTiO_3$(*54*)]. On the contrary, conventional substrates, such as oxides (including VO_2), do not have a good wetting. Therefore, direct growth of $CsPbBr_3$ on tilted VO_2 nanowire on sapphire is relatively challenging so far, and only a minimal amount of growth can be achieved. To solve this problem, we transfer the VO_2 nanowire to a more perovskite-friendly substrate so that the overall nucleation can be facilitated. Hence, the chance for $CsPbBr_3$ to nucleate on VO_2 also increases. The transfer process does prove to help the overall growth because we see that an entire flake can now be grown on a VO_2 beam (fig. S6C). Hypothetically, with the $CsPbBr_3$/VO_2 hybrid material, the semiconducting halide perovskite is supposed to undergo an abrupt compressive strain at the MIT temperature of VO_2. The compressive strain, depending on the value, would significantly affect the lattice and electronic structure of the perovskite, and the strain effect is shown schematically in Fig. 4A. According to the previous report (*50*, *55*, *56*), a moderate compressive strain would contract the Pb–X bond and entail a red shift of the bandgap, whereas upon further increasing the strain value, the PbX_4 octahedron undergoes relative rotation and ends up with a buckling of the X–Pb–X bonding angle, which affects the overlapping of the electron cloud and would, by contrast, increase the bandgap. Consistent with the previous indexing of the two phases of the methylammonium (MA) perovskite (*50*), we name the original phase of $CsPbBr_3$ as α and the new phase under compressive strain as β. To better visualize the hybrid material, we chose relatively large VO_2 microbeams and also a relatively thick $CsPbBr_3$ flake where the domain structure can easily be observed. Figure S6 (A and B) shows the growth of $CsPbBr_3$ flakes

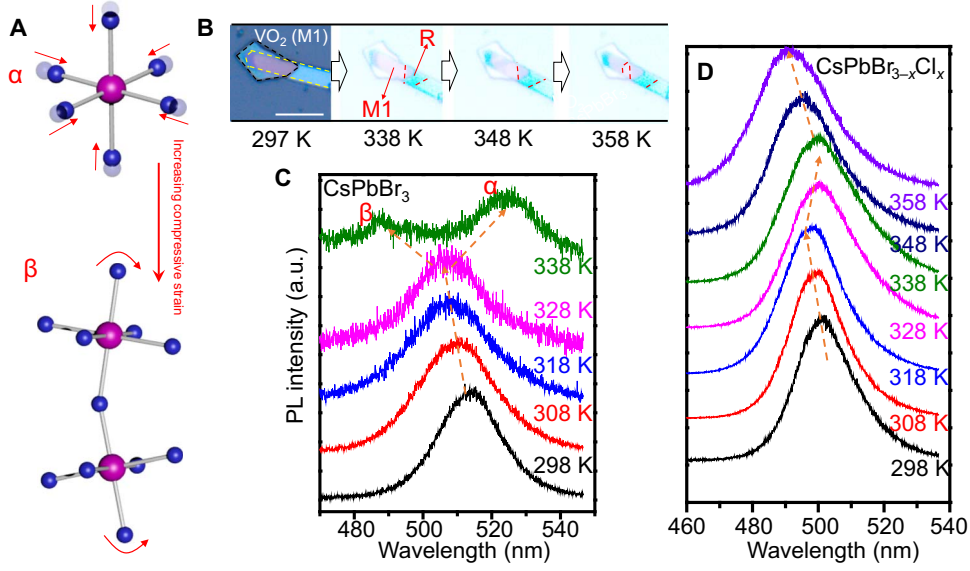

Fig. 4. Strain engineering of heterogeneous soft crystals via $VO_{2\pm\delta}$. (**A**) Schematics showing the structural change of the halide perovksite upon compressive strain. With increasing compressive strain, a phase change (α to β) with the relative octahedral rotation will occur. The phase transition of perovskite will end up with a larger bandgap that is contradictory to the trend of the conventional Pb-X contraction in the α phase. The indexing of the two phases is based on the previous study on MA-based perovskite (*50*). (**B**) Optical image of the VO_2/$CsPbBr_3$ hybrid material with changing temperature. Despite the existence of the growth layer, the appearance of the metallic domain (marked by letter R) and their propagation with increasing temperature can still be observed. Scale bar, 10 μm. (**C**) Temperature-dependent PL spectra of the $CsPbBr_3$ crystal grown on VO_2 where an abnormal PL shift and peak splitting can be observed at the MIT of VO_2. This $CsPbBr_3$ flake under investigation is a small crystallite instead of the large flake shown in (B). (**D**) Similar temperature-dependent PL spectra of a mixed $CsPbBr_{3-x}Cl_x$ crystal on VO_2. The same abnormal PL red shift at the MIT of VO_2 can be observed, whereas the PL shift trend returns to normal after the MIT transition, as indicated by the dashed arrows.

on VO_2, where the square-like morphology of the $CsPbBr_3$ ensures the single crystallinity of the crystal. As shown by fig. S6A, bright photoluminescence (PL) can still be observed as a 405-nm laser is focused onto a small $CsPbBr_3$ crystallite. Despite the submicron size, with the aid of the shape of the bright PL spot, we can still observe the square morphology. The temperature-dependent phase change of the hybrid material (VO_2 outlined by the yellow line and $CsPbBr_3$ by the black line when the sample is at 297 K) is shown in Fig. 4B. $CsPbBr_3$ nanowires can also be grown on thinner VO_2 nanowires, as shown by fig. S6C. With increasing temperature, the metallic domains of VO_2 (highlighted by letter R, and the domain wall is outlined by the red line) gradually appear even at the location where $CsPbBr_3$ is grown. Note that for Fig. 4D, the phase transition of VO_2 seems to be M1-R without the M2 phase observed previously, derived on the basis of the acute angle of the domain boundary (*57*). Basically, an M1-R domain wall will end up with an acute angle, whereas an M2-R domain wall will end up with a right angle. We attribute the phenomena to two possible causes: (i) The presence of a coating layer at high growth temperature provides additional constraint to VO_2. During the cooling process of the growth of perovskite, the presence of coating would hinder VO_2's transition from metallic to insulating and produce a surface compressive strain (because the lattice expands from metallic to insulating for VO_2). According to the phase diagram in Fig. 1A, a compressive strain would lower the MIT temperature and eliminate the M2 phase. (ii) The high growth temperature of perovskite in vacuum may result in oxygen loss that balances the stoichiometric ratio of VO_2. Nonetheless, the MIT phase transition can still be observed and how it modulates the optical properties of perovskite will be further revealed in Fig. 4C.

Figure 4C shows the temperature-dependent PL change of the small crystallite in fig. S6A where the PL peak position initially blue shifts (from 513 to 507 nm) with increasing temperature until 338 K where an abrupt split of peaks (488 and 525 nm) is observed. PL is chosen as a primary tool for detecting the strain in halide perovskite instead of the Raman spectrum due to the soft vibrational bonds and the indistinctive Raman signal at high temperature for halide perovskite. The initial blue shift is consistent with the temperature-dependent bandgap change nature of the perovskite family, whereas the sudden change at 338 K is largely unusual. We attribute the low energy peak at 338 K to be a result of the compressive strain–induced red shift of α-phase perovskite and the high energy peak to be the result of the β phase. In other words, the MIT in VO_2 induces a strain large enough to trigger another phase transition in the perovskite to enable a coexistence of both α and β phases. In addition, from the pure blue shift from 298 to 328 K caused by thermal expansion and the previous study on the linear thermal expansion coefficient of $CsPbBr_3$ (*24*), we are able to determine the shift of bandgap to be around 84.3 meV for each percentage of strain (that is, the deformation potential is 8.43 eV). In that case, the abrupt red shift of 83.8 meV in bandgap for the α phase at MIT corresponds to ~1.0% of compressive strain. The value is very close to the contraction of VO_2 along the *c* axis when the MIT happens. For some other small crystallites such as the case in Fig. 4C, we only observe the β phases (or a strained α phase) as a result of MIT (fig. S7). As the flake grows thicker, the strain transfer at MIT becomes less efficient, and only the red shift of the α phase can be seen, as shown in fig. S8. In addition, we notice that if we increase the nucleation rate, then a fully covered $CsPbBr_3/VO_2$ hybrid material can be obtained as well, only at a cost of smaller straining effect due to the larger thickness and probably decreased crystallinity (fig. S9). Figure 4D continues to show the temperature-dependent PL of a $CsPbBr_{3-x}Cl_x$-mixed halide perovskite grown on VO_2. The alloying of Cl is realized by partially evaporating the NaCl substrate during the growth process. It can be seen that apart from the overall blue shift of PL peaks due to Cl alloying, an abnormal red shift at 328 to 338 K is also present that is the direct consequence of MIT of VO_2. As another solid proof for the MIT-induced strain engineering at an even higher temperature, the PL peak returns to the normal shift trend that solely comes from thermal expansion. We also note that the intensity decrease is different for the case of $CsPbBr_3$ and $CsPbBr_xCl_{3-x}$, with a more significant decrease in the former. The reduction in PL intensity is typical for all semiconductors at higher temperature because the intensity usually decreases exponentially with temperature. We believe that the difference in the decay of the $CsPbBr_3$ and $CsPbBr_xCl_{3-x}$ case is a result of the crystal size. The $CsPbBr_3$ in Fig. 4C is a small crystallite that has the most strain transfer efficiency (we see the β phase). Therefore, when metallic VO_2 forms, the photogenerated carriers will be possibly quenched to a large extent by the VO_2, thus causing the more significant decrease in PL intensity. For the $CsPbBr_xCl_{3-x}$ case, however, the crystal is larger and thicker than that of $CsPbBr_3$. As a result, the strain transfer is less efficient (β phase cannot be reached), and the PL quenching is less significant, leading to a less decreased PL intensity. The strain engineering on $CsPbBr_{3-x}Cl_x$ also shows that the VO_2 can be used broadly as a substrate for dynamic strain engineering with minor limitation on the lattice constant. The cases of $CsPbBr_3$ and $CsPbBr_{3-x}Cl_x$ together show that VO_2 and halide perovskite can form a heterogeneous interface that can be effectively used as a means of strain engineering. To better validate all of our observations, we conducted a control experiment of temperature-dependent PL of halide perovskites flake ($CsPbBr_3$ and $CsPbBr_xCl_{3-x}$), as shown in fig. S10. In both cases, we observed a uniform blue shift of PL peak with increasing temperature, which is consistent with the common observation of halide perovskite, thus serving as a good control experiment of the results presented in Fig. 4C. We also rule out the possibility of the higher energy PL peak in Fig. 4C resulting from degradation at higher temperature. Our control experiment shows very well that both kinds of halide perovskite are very stable up to 373 K without any sign of degradation in PL signal. The control experiment of $CsPbBr_3$ was performed in an order that the flake was heated to 398 K to obtain the first spectrum and then gradually cooled down to room temperature. The flake did not show any sign of degradation after heating. Moreover, the creation of β phase perovskite is only seen in some but not all strain engineering cases, although for all cases, the temperature is raised to the same high level. This indicates that it is the different strain transfer value from VO_2 rather than degradation that causes some halide perovskite to go to β phase. As a final proof for nondegradation, most halide perovskites on VO_2 show an abrupt red shift of PL at the MIT of VO_2, a shift in opposite direction to the possible degradation of $CsPbBr_3$.

DISCUSSION

The presence of ~1% strain and the emergence of both structural and optical phase transitions in halide perovskite under this strain value caused by VO_2's MIT suggest that substantial strain engineering is possible in the material, which forms an incoherent heterogeneous interface with the host substrate. Despite the significant strain value observed, it is still yet to be revealed how the strain is transferred between a heterogeneous interface between two totally dissimilar materials,

and a more fundamental understanding is also needed on the quantitative correlation among the mechanical properties, interface, and the effectiveness of the strain transfer. With this knowledge, it would then be possible to apply the idea to other material systems that are equally technically important and strain-sensitive.

In conclusion, we have, for the first time, achieved the epitaxial growth of a defect-engineered $VO_{2\pm\delta}$ nanowire array and demonstrated strain-induced structural and optical phase transitions in halide perovskite under significant strain enabled by $VO_{2\pm\delta}$'s MIT out of heterogeneous interface. The stoichiometric defect is taken advantage of to engineer the phase transition pathway of the as-grown $VO_{2\pm\delta}$, which could yield a more abrupt lattice contraction at MIT. The fundamental understanding on the growth kinetics of $VO_{2\pm\delta}$ would shed light on the nanowire synthesis technique involving low vapor pressure metals where the VLS method does not apply. By synthesizing soft halide perovskite $CsPbBr_3$ onto VO_2, we showed that by using the MIT of VO_2, a dynamical strain as significant as ~1% can be readily achieved, which is large enough for the perovskite itself to undergo a PbX_6 octahedral tilting–associated structural/optical phase transition. The successful demonstration of the epitaxial phase transition nanowire array suggests an alternative solution to nanocomposites in enabling bulk strain. The study indicates a promising route toward straining heterogeneous materials with the absence of coherent interface.

MATERIALS AND METHODS

Chemical vapor deposition synthesis of VO_2 nanoforest

V_2O_5 powder (99%; Sigma-Aldrich) was placed in a furnace heating center with the heating temperature controlled at around 1143 K. r-Plane sapphire after acetone-ethanol–deionized water cleaning was placed in the downstream about 5 cm away from the precursor. Before deposition, the base pressure of the system was pumped to 0.5 torr, after which 100 standard cubic centimeter per minute (SCCM) of oxygen/argon (20:80%) mixture gas was flowed to maintain the pressure at 1 torr before deposition. The chamber temperature rose from room temperature to the deposition temperature rapidly in 15 min. The first stage of the deposition process lasted for 30 min, after which 100 SCCM of pure argon was flowed for another 5 min, during which the furnace temperature was maintained at 1123 K. The furnace was then quenched down to around 473 K before the r-plane sapphire substrates were taken out.

Chemical vapor deposition synthesis of inorganic halide perovskite $CsPbBr_3$ on VO_2

Powdered cesium bromide (CsBr; 99%; Sigma-Aldrich) was placed in the furnace heating center with the heating temperature controlled at around 773 K, whereas lead(II) bromide ($PbBr_2$; 99%; Sigma-Aldrich) was placed about 10 cm away from the cesium halide in the upper stream due to its lower melting point. Mica/freshly cleaved NaCl substrates with mechanically transferred VO_2 nanowires were placed in the downstream about 10 cm away from the heating zone. The deposition of halide perovskite was performed at a pressure of 160 torr for 15 min.

Microscopy characterization

Morphology of the halide perovskite/VO_2 hybrid material was characterized by a Nikon Eclipse Ti-S inverted optical microscope. TEM JEOL JEM-2010 was used to characterize the crystallographic information of the VO_2. SEM FEI Versa 3D was used for characterizing the VO_2 nanoforest growth and understanding its growth mechanism.

Raman spectroscopy characterization, Raman, and PL mapping

Vibrational modes of the VO_2 nanoforest with different phases were obtained from Raman spectra collected using a Witec alpha300 confocal Raman microscope with an excitation source of continuous wave (cw) 532 nm under magnification of ×100. The temperature-dependent Raman spectra were obtained from a Renishaw Raman microscope with a cw 514-nm laser with an objective lens of 50×. The control of the temperature was performed by using a cryostat.

Photoluminescence characterization

The PL characterization was performed via a customized PL system consisting of a Picoquant 405-nm pulsed laser with a 2-mW power, the same optical microscope that focuses the laser via a 50× objective lens, a Princeton Instruments SP-2358 spectrograph, and a Thorlabs 4 Megapixel Monochrome Scientific CCD (charge-coupled device) Camera.

Temperature-dependent PL characterization

Temperature-dependent PL was carried out by hooking the sample in an INSTEC HCS302 microscope cryostat that can tune the temperature by a MK2000 temperature controller. The cryostat was put under the microscope to get the PL spectrum at each temperature.

X-ray diffraction and pole figure characterization

X-ray diffraction characterization was conducted with a Bruker D8 Discover x-ray diffractometer (Cu Kα = 1.54 Å). A θ-2θ scan was collected with a 0.1-mm incident beam slit and a 0.2-mm detector slit to achieve high resolution. Pole figures were collected with beam and detector slits of both 0.6 mm to maximize signal intensity. During pole figure collection, θ and 2θ were fixed for the targeted reflection, whereas polar angle (χ) was increased from 0° to 88° with 1° increment. At each χ, the azimuthal (ϕ) angle was swept from 0° to 358° with a step size of 2°.

SUPPLEMENTARY MATERIALS

Supplementary material for this article is available at http://advances.sciencemag.org/cgi/content/full/4/5/eaar3679/DC1

fig. S1. SEM image of VO_2 nanoforest obtained at lower substrate temperature during the second stage of growth.

fig. S2. SEM image of VO_2 nanoforest obtained at a higher substrate temperature during the second stage of growth.

fig. S3. SEM and TEM image of VO_2 nanoforest coated with $BaTiO_3$ by room temperature RF sputtering.

fig. S4. TEM characterization of the VO_2-$BaTiO_3$ core-shell structure.

fig. S5. Raman spectra of the pristine VO_2 nanowire (black) and the VO_2 nanowire coated with $BaTiO_3$.

fig. S6. Optical microscope image of single-crystalline $CsPbBr_3$ flake on VO_2.

fig. S7. Temperature-dependent PL spectra of a small crystallite on a thin (~200 nm in diameter) VO_2 nanowire.

fig. S8. Temperature-dependent PL spectra of a $CsPbBr_3$ flake with larger thickness on a VO_2 micron beam.

fig. S9. Temperature-dependent PL spectra of a VO_2 nanowire completely coated with $CsPbBr_3$.

fig. S10. Temperature-dependent PL spectra of $CsPbBr_xCl_{3-x}$ and $CsPbBr_3$ flakes on mica as a control experiment for halide perovskite/VO_2 hybrid structure.

REFERENCES AND NOTES

1. J. Li, Z. Shan, E. Ma, Elastic strain engineering for unprecedented materials properties. *MRS Bull.* **39**, 108–114 (2014).
2. S. Liu, Y. Kim, L. Z. Tan, A. M. Rappe, Strain-induced ferroelectric topological insulator. *Nano Lett.* **16**, 1663–1668 (2016).

3. I. Bozovic, G. Logvenov, I. Belca, B. Narimbetov, I. Sveklo, Epitaxial strain and superconductivity in $La_{2-x}Sr_xCuO_4$ thin films. *Phys. Rev. Lett.* **89**, 107001 (2002).
4. J. H. Lee, L. Fang, E. Vlahos, X. Ke, Y. W. Jung, L. F. Kourkoutis, J.-W. Kim, P. J. Ryan, T. Heeg, M. Roeckerath, V. Goian, M. Bernhagen, R. Uecker, P. C. Hammel, K. M. Rabe, S. Kamba, J. Schubert, J. W. Freeland, D. A. Muller, C. J. Fennie, P. Schiffer, V. Gopalan, E. Johnston-Halperin, D. G. Schlom, A strong ferroelectric ferromagnet created by means of spin-lattice coupling. *Nature* **466**, 954–958 (2010).
5. D. G. Schlom, L.-Q. Chen, C.-B. Eom, K. M. Rabe, S. K. Streiffer, J.-M. Triscone, Strain tuning of ferroelectric thin films. *Annu. Rev. Mater. Res.* **37**, 589–626 (2007).
6. A. J. Hauser, E. Mikheev, N. E. Moreno, J. Hwang, J. Y. Zhang, S. Stemmer, Correlation between stoichiometry, strain, and metal-insulator transitions of $NdNiO_3$ films. *Appl. Phys. Lett.* **106**, 092104 (2015).
7. B. Yildiz, "Stretching" the energy landscape of oxides—Effects on electrocatalysis and diffusion. *MRS Bull.* **39**, 147–156 (2014).
8. S. W. Bedell, A. Khakifirooz, D. K. Sadana, Strain scaling for CMOS. *MRS Bull.* **39**, 131–137 (2014).
9. E. Yablonovitch, E. O. Kane, Band structure engineering of semiconductor lasers for optical communications. *J. Lightwave Technol.* **6**, 1292–1299 (1988).
10. A. R. Adams, Strained-layer quantum-well lasers. *IEEE J. Sel. Topics Quantum Electron.* **17**, 1364–1373 (2011).
11. R. Pillarisetty, B. Chu-Kung, S. Corcoran, G. Dewey, J. Kavalieros, H. Kennel, R. Kotlyar, V. Le, D. Lionberger, M. Metz, N. Mukherjee, J. Nah, W. Rachmady, M. Radosavljevic, U. Shah, S. Taft, H. Then, N. Zelick, R. Chau, High mobility strained germanium quantum well field effect transistor as the p-channel device option for low power (Vcc = 0.5 V) III–V CMOS architecture, in *Electron Devices Meeting (IEDM), 2010 IEEE International* (IEEE, 2010), pp. 6–7.
12. T. Zhu, J. Li, S. Ogata, S. Yip, Mechanics of ultra-strength materials. *MRS Bull.* **34**, 167–172 (2009).
13. W. D. Nix, Mechanical properties of thin films. *Metall. Trans. A* **20**, 2217–2245 (1989).
14. D. W. Pashley, The study of epitaxy in thin surface films. *Adv. Phys.* **5**, 173–240 (1956).
15. R. Vincent, An analysis of the residual strains in epitaxial tin films. *Philos. Mag.* **19**, 1127–1139 (1969).
16. A. Chen, J.-M. Hu, P. Lu, T. Yang, W. Zhang, L. Li, T. Ahmed, E. Enriquez, M. Weigand, Q. Su, H. Wang, J.-X. Zhu, J. L. MacManus-Driscoll, L.-Q. Chen, D. Yarotski, Q. Jia, Role of scaffold network in controlling strain and functionalities of nanocomposite films. *Sci. Adv.* **2**, e1600245 (2016).
17. S. Hao, L. Cui, D. Jiang, X. Han, Y. Ren, J. Jiang, Y. Liu, Z. Liu, S. Mao, Y. Wang, Y. Li, X. Ren, X. Ding, S. Wang, C. Yu, X. Shi, M. Du, F. Yang, Y. Zheng, Z. Zhang, X. Li, D. E. Brown, J. Li, A transforming metal nanocomposite with large elastic strain, low modulus, and high strength. *Science* **339**, 1191–1194 (2013).
18. J. L. MacManus-Driscoll, P. Zerrer, H. Wang, H. Yang, J. Yoon, A. Fouchet, R. Yu, M. G. Blamire, Q. Jia, Strain control and spontaneous phase ordering in vertical nanocomposite heteroepitaxial thin films. *Nat. Mater.* **7**, 314–320 (2008).
19. J.-F. Ge, Z.-L. Liu, C. Liu, C.-L. Gao, D. Qian, Q.-K. Xue, Y. Liu, J.-F. Jia, Superconductivity above 100 K in single-layer FeSe films on doped $SrTiO_3$. *Nat. Mater.* **14**, 285–289 (2015).
20. S. Tan, Y. Zhang, M. Xia, Z. Ye, F. Chen, X. Xie, R. Peng, D. Xu, Q. Fan, H. Xu, J. Jiang, T. Zhang, X. Lai, T. Xiang, J. Hu, B. Xie, D. Feng, Interface-induced superconductivity and strain-dependent spin density waves in FeSe/$SrTiO_3$ thin films. *Nat. Mater.* **12**, 634–640 (2013).
21. R. Peng, H. C. Xu, S. Y. Tan, H. Y. Cao, M. Xia, X. P. Shen, Z. C. Huang, C. H. P. Wen, Q. Song, T. Zhang, B. P. Xie, X. G. Gong, D. L. Feng, Tuning the band structure and superconductivity in single-layer FeSe by interface engineering. *Nat. Commun.* **5**, 5044 (2014).
22. D. Kucharczyk, T. Niklewski, Accurate x-ray determination of the lattice parameters and the thermal expansion coefficients of VO_2 near the transition temperature. *J. Appl. Crystallogr.* **12**, 370–373 (1979).
23. N. F. Mott, L. Friedman, Metal-insulator transitions in VO_2, Ti_2O_3 and $Ti_{2-x}V_xO_3$. *Philos. Mag.* **30**, 389–402 (1974).
24. Y. Rakita, S. R. Cohen, N. K. Kedem, G. Hodes, D. Cahen, Mechanical properties of $APbX_3$ (A=Cs or CH_3NH_3; X=I or Br) perovskite single crystals. *MRS Commun.* **5**, 623–629 (2015).
25. C. Grote, R. F. Berger, Strain tuning of tin–halide and lead–halide perovskites: A first-principles atomic and electronic structure study. *J. Phys. Chem. C* **119**, 22832–22837 (2015).
26. L. Leppert, S. E. Reyes-Lillo, J. B. Neaton, Electric field-and strain-induced Rashba effect in hybrid halide perovskites. *J. Phys. Chem. Lett.* **7**, 3683–3689 (2016).
27. V. G. Dubrovskii, N. V. Sibirev, G. E. Cirlin, J. C. Harmand, V. M. Ustinov, Theoretical analysis of the vapor-liquid-solid mechanism of nanowire growth during molecular beam epitaxy. *Phys. Rev. E* **73**, 021603 (2006).
28. V. G. Dubrovskii, Chapter one-theory of VLS growth of compound semiconductors. *Semicond. Semimetals* **93**, 1–78 (2015).
29. M. Imada, A. Fujimori, Y. Tokura, Metal-insulator transitions. *Rev. Mod. Phys.* **70**, 1039 (1998).
30. S. Lee, C. Cheng, H. Guo, K. Hippalgaonkar, K. Wang, J. Suh, K. Liu, J. Wu, Axially engineered metal–insulator phase transition by graded doping VO_2 nanowires. *J. Am. Chem. Soc.* **135**, 4850–4855 (2013).
31. J. H. Park, J. M. Coy, T. S. Kasirga, C. Huang, Z. Fei, S. Hunter, D. H. Cobden, Measurement of a solid-state triple point at the metal–insulator transition in VO_2. *Nature* **500**, 431–434 (2013).
32. N.-G. Park, M. Grätzel, T. Miyasaka, K. Zhu, K. Emery, Towards stable and commercially available perovskite solar cells. *Nat. Energy* **1**, 16152 (2016).
33. M. A. Green, A. Ho-Baillie, H. J. Snaith, The emergence of perovskite solar cells. *Nat. Photonics* **8**, 506–514 (2014).
34. H. Zhu, Y. Fu, F. Meng, X. Wu, Z. Gong, Q. Ding, M. V. Gustafsson, M. T. Trinh, S. Jin, X.-Y. Zhu, Lead halide perovskite nanowire lasers with low lasing thresholds and high quality factors. *Nat. Mater.* **14**, 636–642 (2015).
35. F. Li, C. Ma, H. Wang, W. Hu, W. Yu, A. D. Sheikh, T. Wu, Ambipolar solution-processed hybrid perovskite phototransistors. *Nat. Commun.* **6**, 8238 (2015).
36. H. Wei, Y. Fang, P. Mulligan, W. Chuirazzi, H.-H. Fang, C. Wang, B. R. Ecker, Y. Gao, M. A. Loi, L. Cao, J. Huang, Sensitive x-ray detectors made of methylammonium lead tribromide perovskite single crystals. *Nat. Photonics* **10**, 333–339 (2016).
37. W. Wei, Y. Zhang, Q. Xu, H. Wei, Y. Fang, Q. Wang, Y. Deng, T. Li, A. Gruverman, L. Cao, J. Huang, Monolithic integration of hybrid perovskite single crystals with heterogenous substrate for highly sensitive x-ray imaging. *Nat. Photonics* **11**, 315–321 (2017).
38. Z.-K. Tan, R. S. Moghaddam, M. L. Lai, P. Docampo, R. Higler, F. Deschler, M. Price, A. Sadhanala, L. M. Pazos, D. Credgington, F. Hanusch, T. Bein, H. J. Snaith, R. H. Friend, Bright light-emitting diodes based on organometal halide perovskite. *Nat. Nanotechnol.* **9**, 687–692 (2014).
39. Y. Cheng, T. Zhang, Y. Cai, K. M. Ho, K. K. Fung, N. Wang, Structure and metal-to-insulator transition of VO_2 nanowires grown on sapphire substrates. *Eur. J. Inorg. Chem.* **2010**, 4332–4338 (2010).
40. B. S. Guiton, Q. Gu, A. L. Prieto, M. S. Gudiksen, H. Park, Single-crystalline vanadium dioxide nanowires with rectangular cross sections. *J. Am. Chem. Soc.* **127**, 498–499 (2005).
41. J. M. Atkin, S. Berweger, E. K. Chavez, M. B. Raschke, J. Cao, W. Fan, J. Wu, Strain and temperature dependence of the insulating phases of VO_2 near the metal-insulator transition. *Phys. Rev. B* **85**, 020101 (2012).
42. J. P. Pouget, H. Launois, T. M. Rice, P. Dernier, A. Gossard, G. Villeneuve, P. Hagenmuller, Dimerization of a linear Heisenberg chain in the insulating phases of V_{1-x} Cr_xO_2. *Phys. Rev. B* **10**, 1801 (1974).
43. M. H. Kim, B. Lee, S. Lee, C. Larson, J. M. Baik, C. T. Yavuz, S. N. Seifert, S. Vajda, R. E. Winans, M. Moskovits, G. D. Stucky, A. M. Wodtke, Growth of metal oxide nanowires from supercooled liquid nanodroplets. *Nano Lett.* **9**, 4138–4146 (2009).
44. J. Y. Chou, J. L. Lensch-Falk, E. R. Hemesath, L. J. Lauhon, Vanadium oxide nanowire phase and orientation analyzed by Raman spectroscopy. *J. Appl. Phys.* **105**, 034310 (2009).
45. Z. Tao, F. Zhou, T.-R. T. Han, D. Torres, T. Wang, N. Sepulveda, K. Chang, M. Young, R. R. Lunt, C.-Y. Ruan, The nature of photoinduced phase transition and metastable states in vanadium dioxide. *Sci. Rep.* **6**, 38514 (2016).
46. H. W. Yang, J. I. Sohn, J. H. Yang, J. E. Jang, S. N. Cha, J. Kim, D. J. Kang, Unusual M_2-mediated metal-insulator transition in epitaxial VO_2 thin films on GaN substrates. *EPL* **109**, 27004 (2015).
47. J. I. Sohn, H. J. Joo, K. S. Kim, H. W. Yang, A.-R. Jang, D. Ahn, H. H. Lee, S. Cha, D. J. Kang, J. M. Kim, Stress-induced domain dynamics and phase transitions in epitaxially grown VO_2 nanowires. *Nanotechnology* **23**, 205707 (2012).
48. P. Schilbe, Raman scattering in VO_2. *Physica B Condens. Matter.* **316**, 600–602 (2002).
49. J. L. Routbort, D. Singh, P. K. Dutta, R. Ramasamy, J. V. Spirig, S. Akbar, "High-temperature potentiometric oxygen sensor with internal reference," U.S. Patent 8,057,652 (2011).
50. A. Jaffe, Y. Lin, C. M. Beavers, J. Voss, W. L. Mao, H. I. Karunadasa, High-pressure single-crystal structures of 3D lead-halide hybrid perovskites and pressure effects on their electronic and optical properties. *ACS Cent. Sci.* **2**, 201–209 (2016).
51. Y. Wang, X. Sun, R. Shivanna, Y. Yang, Z. Chen, Y. Guo, G.-C. Wang, E. Wertz, F. Deschler, Z. Cai, H. Zhou, T.-M. Lu, J. Shi, Photon transport in one-dimensional incommensurately epitaxial $CsPbX_3$ arrays. *Nano Lett.* **16**, 7974–7981 (2016).
52. Y. Wang, Y. Shi, G. Xin, J. Lian, J. Shi, Two-dimensional van der Waals epitaxy kinetics in a three-dimensional perovskite halide. *Cryst. Growth Des.* **15**, 4741–4749 (2015).
53. Y. Wang, X. Sun, Z. Chen, Y.-Y. Sun, S. Zhang, T.-M. Lu, E. Wertz, J. Shi, High-temperature ionic epitaxy of halide perovskite thin film and the hidden carrier dynamics. *Adv. Mater.* **29**, 1702643 (2017).
54. J. Chen, D. J. Morrow, Y. Fu, W. Zheng, Y. Zhao, L. Dang, M. J. Stolt, D. D. Kohler, X. Wang, K. J. Czech, M. P. Hautzinger, S. Shen, L. Guo, A. Pan, J. C. Wright, S. Jin, Single-crystal thin films of cesium lead bromide perovskite epitaxially grown on metal oxide perovskite ($SrTiO_3$). *J. Am. Chem. Soc.* **139**, 13525–13532 (2017).
55. A. Jaffe, Y. Lin, H. I. Karunadasa, Halide perovskites under pressure: Accessing new properties through lattice compression. *ACS Energy Lett.* **2**, 1549–1555 (2017).

56. D. Umeyama, Y. Lin, H. I. Karunadasa, Red-to-black piezochromism in a compressible Pb–I–SCN layered perovskite. *Chem. Mater.* **28**, 3241–3244 (2016).
57. T. Favaloro, J. Suh, B. Vermeersch, K. Liu, Y. Gu, L.-Q. Chen, K. X. Wang, J. Wu, A. Shakouri, Direct observation of nanoscale Peltier and Joule effects at metal–insulator domain walls in vanadium dioxide nanobeams. *Nano Lett.* **14**, 2394–2400 (2014).

Acknowledgments
Funding: This material is based upon work supported by the Rensselaer Polytechnic Institute Presidential Graduate Fellowship and the Air Force Office of Scientific Research under award number FA9550-18-1-0116. The structural measurements are also supported by the NYSTAR Focus Center under award number C130117, the NSF under award number CMMI 1635520 and the nanoprobe beamline of Advanced Photon Source operated by the Center of Nanoscale Materials of the Argonne National Laboratory. **Author contribution:** J.S. conceived the study. Y.W. and Z.C. performed the growth and all the optical characterizations. Y.W. and X.S. performed the structural characterization. All the authors analyzed the data and wrote the manuscript. **Competing interests:** The authors declare that they have no competing interests. **Data and materials availability:** All data needed to evaluate the conclusions in the paper are present in the paper and/or the Supplementary Materials. Additional data related to this paper may be requested from the authors.

Submitted 31 October 2017
Accepted 17 April 2018
Published 25 May 2018
10.1126/sciadv.aar3679

Citation: Y. Wang, X. Sun, Z. Chen, Z. Cai, H. Zhou, T.-M. Lu, J. Shi, Defect-engineered epitaxial $VO_{2\pm\delta}$ in strain engineering of heterogeneous soft crystals. *Sci. Adv.* **4**, eaar3679 (2018).

ScienceAdvances

Defect-engineered epitaxial $VO_{2\pm\delta}$ in strain engineering of heterogeneous soft crystals

Yiping Wang, Xin Sun, Zhizhong Chen, Zhonghou Cai, Hua Zhou, Toh-Ming Lu and Jian Shi

Sci Adv **4** (5), eaar3679.
DOI: 10.1126/sciadv.aar3679